To link to this article: DOI:10.1016/j.optlaseng.2010.01.010
http://dx.doi.org/10.1016/j.optlaseng.2010.01.010

3D mechanical analysis of aeronautical plain bearings: Validation of a finite element model from measurement of displacement fields by digital volume correlation and optical scanning tomography

A. Germaneau [a,*], F. Peyruseigt [b], S. Mistou [c], P. Doumalin [a], J.-C. Dupré [a]

[a] Institut Pprime, CNRS - Université de Poitiers - ENSMA, UPR 3346, S.P.2M.I., Boulevard Marie et Pierre Curie, Téléport 2, BP 30179, 86962 Futuroscope Chasseneuil Cedex, France
[b] Airbus France, TWEYK, E5002, 316, route de Bayonne, 31060 Toulouse Cedex, France
[c] ENI de Tarbes, Laboratoire Génie de Production, 47, avenue d'Azereix, BP1629, 65016 Tarbes Cedex, France

A B S T R A C T

On Airbus aircraft, spherical plain bearings are used on many components; in particular to link engine to pylon or pylon to wing. Design of bearings is based on contact pressure distribution on spherical surfaces. To determine this distribution, a 3D analysis of the mechanical behaviour of aeronautical plain bearing is presented in this paper. A numerical model has been built and validated from a comparison with 3D experimental measurements of kinematic components. For that, digital volume correlation (DVC) coupled with optical scanning tomography (OST) is employed to study the mechanical response of a plain bearing model made in epoxy resin. Experimental results have been compared with the ones obtained from the simulated model. This comparison enables us to study the influence of various boundary conditions to build the FE model. Some factors have been highlighted like the fitting behaviour which can radically change contact pressure distribution. This work shows the contribution of a representative mechanical environment to study precisely mechanical response of aeronautical plain bearings.

Keywords:
DVC
3D measurements
Scattered light
Numerical modelling
Spherical plain bearings

1. Introduction

In this paper, an original approach to characterize mechanical response of a structure with a complex geometry, an aeronautical plain bearing, is presented. This kind of problem which involves three-dimensional local stress repartition must be studied with a three-dimensional simulation. As for any simulation, numerical modelling has to be validated by experimental measurements. In the case of this work, the geometry involves a localized contact problem and surface measurements are not sufficient. This problem can be approached by two experimental measurement methods: scattered light photoelasticity (SLP) [1] and digital volume correlation (DVC) [2–5]. SLP technique has already been employed to study the problem by considering stress repartitions within a resin model specimen [6]. SLP enables us to obtain photoelastic fringes describing the continuous stress field of a mechanical system in real time. However, this method cannot achieve geometry variations of the specimen and a quantitative analysis of stresses remains difficult because only secondary principal stress differences are available. In the present work, another approach, from measurement of kinematic components, is presented by employing DVC to study the 3D mechanical response of aeronautical plain bearings. This latter technique gives evolution of discrete displacement field in the whole volume, i.e. evolution of the geometry, and enables an easier quantitative mechanical analysis and a comparison with a finite element model.

Until A380 program, engine manufacturers of Airbus aircrafts had to design and manufacture engine mounts on aircraft pylons. These elements are very critical for a good mechanical behaviour of the pylon-to-engine link and therefore are equipped with spherical plain bearings (Fig. 1). The role of bearings is to compensate strain of engine mounts and differential thermal expansions between engine and pylon in order to avoid link hyperstaticity that can induce unwanted loads on engine or pylon parts. Since A380 program, Airbus has taken the responsibility for mount conception and wishes to improve its knowledge of mechanical behaviour of plain bearings because scuffing phenomenon on spherical surfaces has been observed. This scuffing is induced by bad slipping conditions of this interface that are linked to contact parameters including surface aspects (geometry, materials, etc.) and also solicitations. In particular, contact pressure distribution is a significant parameter that has to be considering for bearing design in respect to their functionality. In the present case of spherical bearing, Hertz's analytical solution

* Corresponding author.
E-mail addresses: arnaud.germaneau@lms.univ-poitiers.fr (A. Germaneau), francois.peyruseigt@airbus.com (F. Peyruseigt), mistou@enit.fr (S. Mistou).

doi:10.1016/j.optlaseng.2010.01.010

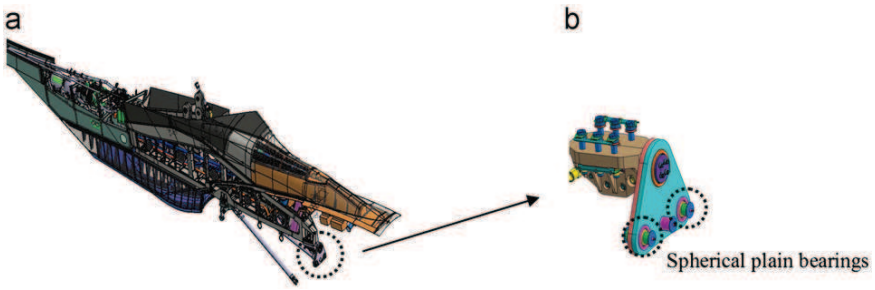

Fig. 1. Airbus A380 engine pylon (a) and bearings equipped items (b).

[7] cannot be employed because of a conformal contact. Traditionally, this kind of contact pressure can be approached with the assumption of projected pressure and the following expression:

$$P = \frac{F}{2RL} \tag{1}$$

where P is the average pressure, F the applied load, R the bearing sphere radius and L the bearing width. This modelling gives a uniform pressure distribution on the whole contact surface and does not involve scuffing problem.

Others models have been developed. An expression based on the assumption that maximum pressure is located at the centre of the contact with an ellipsoidal distribution along bearing width and half-circumference [8] is commonly employed to determine contact pressure distribution according to the spherical coordinates θ and ω (Fig. 2):

$$P(\theta,\omega) = \frac{F}{2(R^2 - L^2/4)\sin^{-1}(L/2R)} \cos\left(\frac{\theta\pi}{2\sin^{-1}(L/2R)}\right)\cos\omega \tag{2}$$

This modelling is based on strong assumptions which must be validated: contact configurations can cause free-edge effects because of the finite length of the contact width and localization of maximal pressure is not assured. These effects have been previously highlighted on surgical hip implant behaviour [9].

To have a better knowledge of bearing behaviour, Airbus want to develop a tool enabling us to determine in a realistic way the contact pressure distribution on the spherical surface of aeronautical plain bearings. The research work has been launched in order to build a model by finite-element method (FEM). FEM enables us study effects of various parameters such as geometry, materials, friction and also to identify those parameters which have significant contributions on the bearing behaviour.

Assumptions and boundary conditions employed to build the numerical model have to be validated from experimental fields obtained during the loading of the bearing. Owing to the spherical geometry of the bearing, a surface measurement is not sufficient to study the mechanical response of the system and so 3D measurements are needed. This work is focused on the 3D experimental approach based on the use of DVC coupled with OST on a demonstrator spherical bearing specimen made in a transparent material.

This applied technique is firstly described in this paper and then experimental results are shown and compared with numerical data obtained from FE model.

2. Digital volume correlation (DVC)

DVC has been developed [2–5] from the 3D extension of digital image correlation technique, usually used in mechanics to measure plane or 3D displacements of loaded surfaces [10–15].

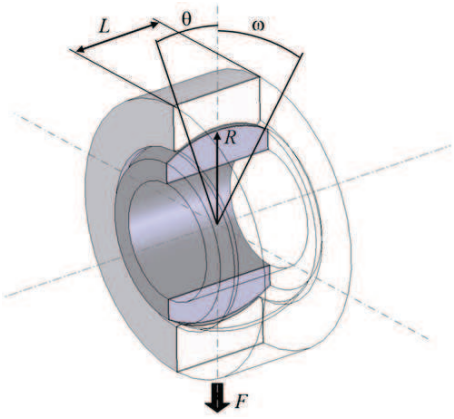

Fig. 2. Spherical plain bearing.

DVC enables to measure a 3D displacement field between a reference state and a deformed state of a studied sample. The displacement of each point of a virtual grid defined in the initial volume image is calculated by intercorrelation of the grey levels of the neighbourhood $\boldsymbol{D}$ surrounding the considered point in both states. $\boldsymbol{D}$ is composed of several voxels and corresponds to a subset of the volume. By noting $\underline{\boldsymbol{X}}$ and $\underline{\boldsymbol{x}}$ the coordinates (in voxels) of a same material point in the reference state and the deformed state, both configurations are linked by the 3D material transformation $\boldsymbol{\phi}$: $\underline{\boldsymbol{x}}=\boldsymbol{\phi}(\underline{\boldsymbol{X}})$. For a subset $\boldsymbol{D}$ centred at the point $\underline{\boldsymbol{X}}_0$ in the reference state, $\boldsymbol{\phi}$ is approximated by its expansion at the first order corresponding to a rigid body motion combined with a homogeneous deformation:

$$\phi(\underline{X}) = \underline{X} + \underline{U}(\underline{X}) = \underline{X} + \underline{U}(\underline{X}_0) + \frac{\partial U}{\partial \underline{X}}(\underline{X}_0) \tag{3}$$

The displacement $\boldsymbol{U}(\underline{\boldsymbol{X}}_0)$ of the subset centre gives the intensity of the rigid body translation. The local displacement gradient expression $\frac{\partial U}{\partial \underline{X}}(\underline{X}_0)$ includes the rigid body rotation and the local stretch of the subset volume. The best values (translation and local gradient) characterizing the material transformation are those which minimize a correlation coefficient $\boldsymbol{C}$ which measures the degree of similarity of grey level distributions in $\boldsymbol{D}$ and its transformed one by $\boldsymbol{\phi}$. The chosen formulation of $\boldsymbol{C}$ is insensitive to small contrast and brightness fluctuations which can appear in images: a normalized cross correlation formulation based on grey level gaps in respect to the average on the subset:

$$C = 1 - \frac{\sum_{\underline{X}\in D}(f(\underline{X}) - \overline{f}_D)(g(\phi(\underline{X})) - \overline{g}_D)}{\sqrt{\sum_{\underline{X}\in D}(f(\underline{X}) - \overline{f}_D)^2}\sqrt{\sum_{\underline{X}\in D}(g(\phi(\underline{X})) - \overline{g}_D)^2}} \tag{4}$$

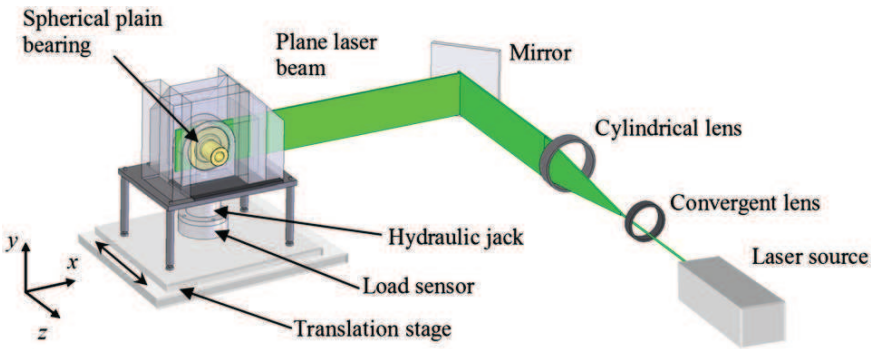

Fig. 3. OST experimental setup.

where $\underline{\boldsymbol{X}}$ refers to voxels in $\boldsymbol{D}$, $\boldsymbol{f}$ and $\boldsymbol{g}$ are, respectively, the grey levels in the initial and deformed images, $\overline{f}_D$ and $\overline{g}_D$ are their averages over $\boldsymbol{D}$ and $\phi(\boldsymbol{D})$.

The determination of the coefficient $\boldsymbol{C}$ and so of final positions $\underline{\boldsymbol{x}}$ is performed by a first-gradient minimization procedure [4,5]. A trilinear interpolation of the grey levels in the deformed image is used in order to calculate the grey level variations between two adjacent voxels. In this way, it is possible to achieve the position of the subset $\boldsymbol{D}$ in fractions of voxels (subvoxel precision).

3. Optical scanning tomography (OST)

3.1. Principle

To investigate 3D models made in transparent materials, a method based on the scattered light phenomenon has been recently developed [4,5]. The scattered light phenomenon is created by including particles, added during the elaboration of the transparent material and randomly distributed in the specimen. A volume image generated by optical scanning tomography (OST) is obtained by optical slicing and scanning the specimen with a plane laser beam in the z-direction (Fig. 3) and a motorized translation stage (with a minimum increment equal to 0.625 μm) controlled by an integrated linear-scale encoder. At each position of the beam, an $\boldsymbol{x}$–$\boldsymbol{y}$ 2D image of the illuminated section is recorded. The volume is constituted by the succession of these 2D images. The plane laser beam is obtained by using a laser source, a convergent lens and a cylindrical lens (Fig. 3). The random distribution of the grey levels within the volume image is given by the scattered light phenomenon. To create this phenomenon, several kinds of particles with different sizes or shapes can be employed. It has been showed [5] that polyamide particles with an around 150 μm is well adapted for 3D structure study.

3.2. Preparation of plain bearing specimens

To study on the mechanical problem of spherical contact, a demonstrator bearing with a standard design (Fig. 4) is considered: shaft, inner and outer rings were casted in an epoxy resin containing polyamide particles. Each part of the bearing is machined (Fig. 5) and a gap of 40 μm is measured between inner and outer ring. To apply a radial load on the bearing fitting with a 20k N hydraulic jack, a specific test device was made in PMMA (Fig. 6). The fitting is made in PMMA in order to avoid any distortion of the light during the scanning of the bearing. The gap between fitting and outer ring is also measured and equal to

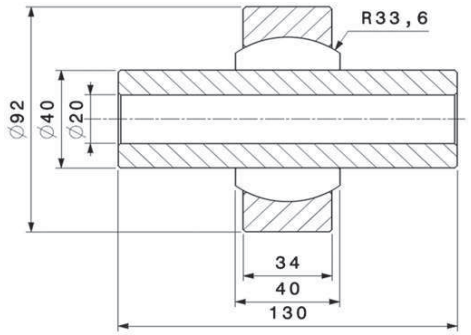

Fig. 4. Design of the demonstrator bearing (dimensions in mm).

100 μm. The shaft extremities are inserted into two PMMA thick plates (Fig. 6). Those plates, with two other ones, create a tank where a liquid having a similar optical index to that of epoxy resin immerses the bearing to avoid reflexion and refraction phenomena. During the elaboration of the material, standard tensile specimens were also casted in order to determine mechanical properties useful to build simulated model. Young's modulus and Poisson's ratio are obtained from the use of the mark tracking technique (Table 1) [17].

4. Experiments

According to the size of the specimen and the used particles, the spatial resolution of volume image is equal to 0.06 mm/voxel. Fig. 7 shows a volume image of the bearing demonstrator specimen obtained by OST at the reference state. Volume images are recorded for two other states: for imposed loads equal to 500 and 1000 daN. The studied zone is the upper part of the bearing (Fig. 7) and a 3D grid of 36,000 points is defined to determine the displacement components within inner and outer rings. Analysis by DVC is performed with a subset volume equal to 31 voxels and with a step of 20 voxels between two adjacent subset volumes. Fig. 8 shows the evolution of displacement components along the three directions for both load states. According to the experimental conditions, particles and materials used, it has been shown from rigid motion tests [4,5] that displacement measurement uncertainty is around 0.1 voxel corresponding to 0.006 mm. On one hand, displacements along the z-direction (U_z) are very low and close to the measurement uncertainty. On the other hand, displacements along x (U_x) and y (U_y) increase with the imposed load. Displacement fields within

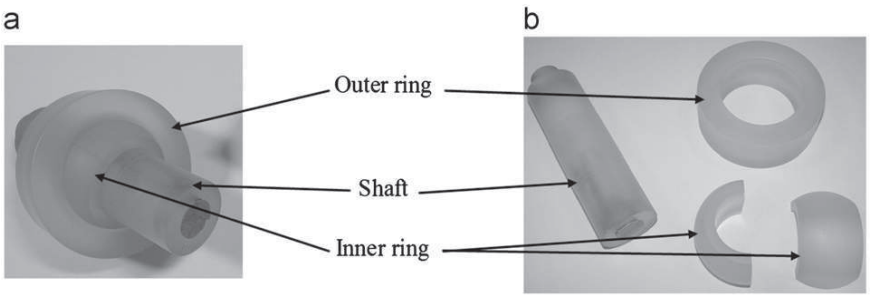

Fig. 5. Epoxy resin replica of the bearing (a) and its elements (b).

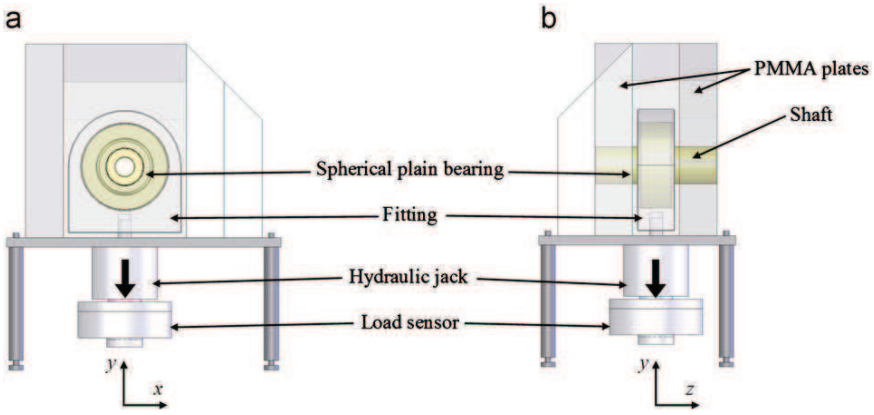

Fig. 6. Loading system according to the x–y plane (a) and to the y–z plane (b).

Table 1
Mechanical characteristics of the materials of epoxy resin samples and PMMA.

	E (MPa)	ν
Epoxy resin containing polyamide powder	2700 ± 15	$0.38 \pm 4 \times 10^{-3}$
PMMA (fitting)	2800 ± 15	$0.38 \pm 4 \times 10^{-3}$

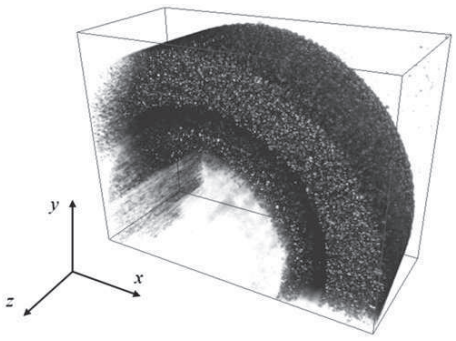

Fig. 7. Volume image of the bearing recorded by OST.

inner and outer rings are similar. There are some aberrant measured points due to partial reflection of the laser beam at the interface between inner and outer rings. According to each side of the shaft, displacements U_x along x in a horizontal median plane are oriented toward the shaft and absolute values go from 0.05 to 0.1 mm. In the upper part of the bearing, displacement along x should be theoretically around zero but it is slightly superior to zero. This may be due to the load which is not exactly symmetrical along the y-axis and according to the geometry. On the sides of the bearing, displacement is larger than the one observed on the upper part and is around 0.3 mm. Displacements values within the outer ring are slightly higher than the ones observed within the inner ring but displacement fields are continuous between each part. Analysis of both loaded states shows that the bearing is compressed according to the y-direction in the upper part between the fitting and the shaft and according to the x-direction on the sides. There is a discontinuity in the displacement fields in the left-hand side of the equatorial plane of the inner ring which can be linked to the splitting of the inner ring. These effects can also be due to the disturbance of the optical path of the laser beam trough the width of the whole bearing during the scanning.

Strain tensor components can be calculated from displacement field [4]. In the present case, strain values remain low and maximum level is around 0.005. This value remains lower than the elastic strain limit of the material (0.02) which shows the latter works in the elastic regime.

5. Numerical modelling

The numerical model of the plain bearing, developed with the commercial software ABAQUS 6.6, is composed with two parts: an outer and an inner ring. In reality, the inner ring is split in two half rings to allow the bearing assembly. In the numerical model, this part is not split. First studies on this bearing modelling show influence of the mechanical environment on its behaviour. Therefore, shaft and bearing fitting are considered too (Fig. 9). Materials of those parts are assumed to have an elastic behaviour.

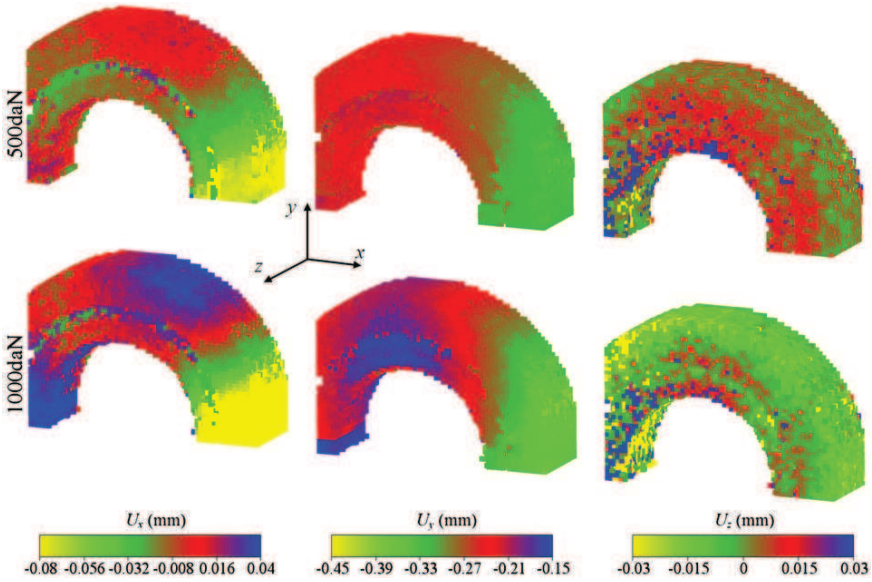

Fig. 8. 3D distribution of displacement components in the bearing for imposed loads equal to 500 and 1000 Da N.

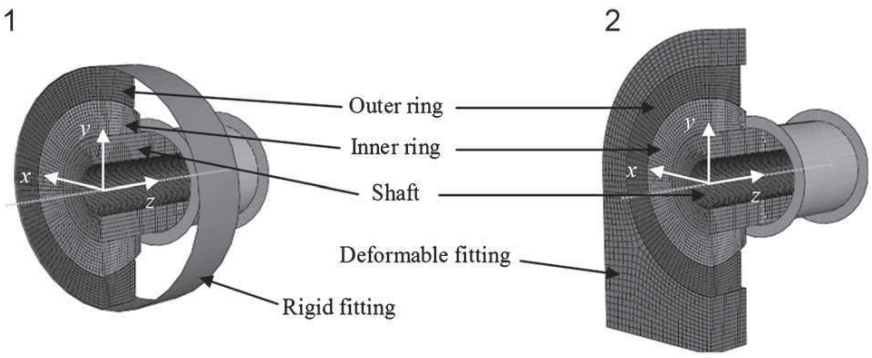

Fig. 9. Simulation of the bearing with a rigid fitting (1) and a deformable fitting (2).

The load is applied on the fitting. Extremities of shaft are locked by cylindrical rigid surfaces. In the simulations, hexahedral first-order reduced-integrated elements (C3D8R) were used because they offer accurate results for analysis of contact problems [16]. Several simulations have been conducted to identify an optimal mesh density. Symmetry can be considered to model a quarter of the bearing (Fig. 10). Four contacts are considered: fitting-on-outer ring contact, outer ring-on-inner ring contact, inner ring-on-shaft contact and shaft-on-rigid surface contact. The first three ones are governed by a Coulomb friction law and last contact is considered frictionless. Many questions remain about assumptions and boundary conditions that can be applied on this model in particular with gaps, rigid fitting and split inner ring considerations.

In this work, two numerical models are studied and are shown in Fig. 9. The first model is built from empirical experience (model 1, Fig. 9) and in particular a rigid fitting and there is no gap between each part of the bearing. The second model (model 2, Fig. 9) is built in accordance with others observations performed by scattered light photoelasticity [6]. This model takes into account deformability of the fitting which is made in PMMA and real measured gaps between bearing elements are considered. Gap between inner and outer rings is equal to 40 μm and it is equal to 100 μm between outer ring and fitting.

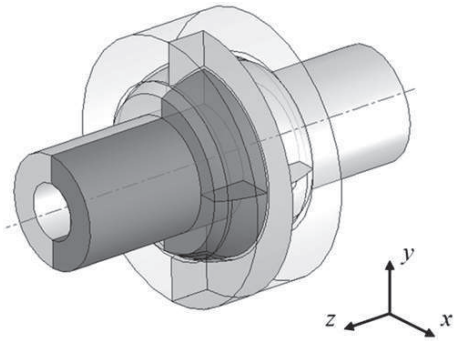

Fig. 10. Simulation of a quarter of the bearing.

Mechanical properties of the materials have been experimentally identified by a mark tracking technique for strain measurement [17] and used for the numerical model (Table 1). The friction coefficient of the Coulomb law is assumed to be equal to 0.3.

Figs. 11 and 12 show the 3D displacement fields obtained by both models for loadings of 500 and 1000 daN. With model 1, displacement field seems to be homogeneous in the whole

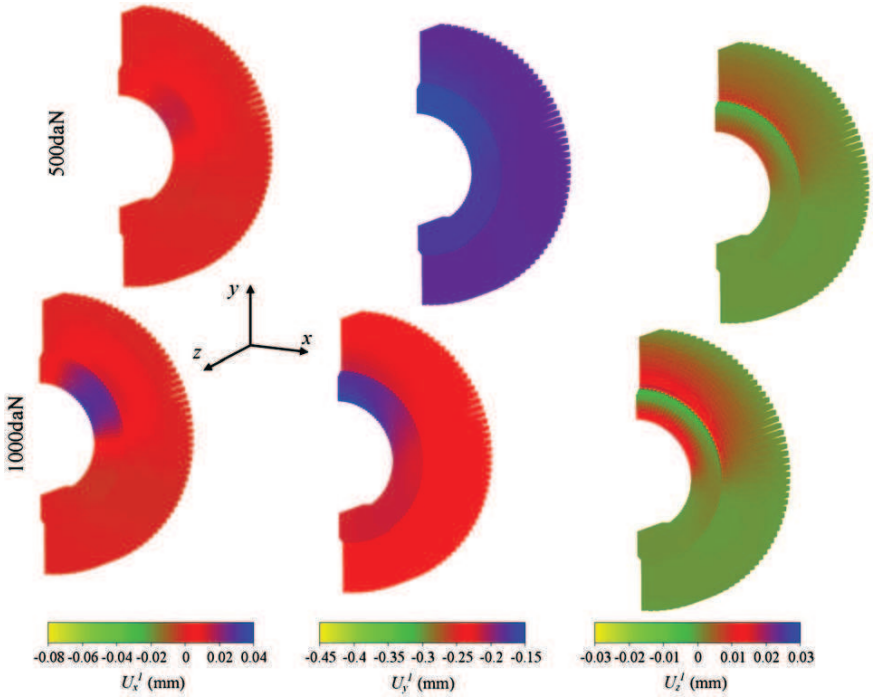

Fig. 11. Distribution of simulated displacement components ($\underline{U}^1$) by considering a rigid fitting and without gaps between each part of the bearing.

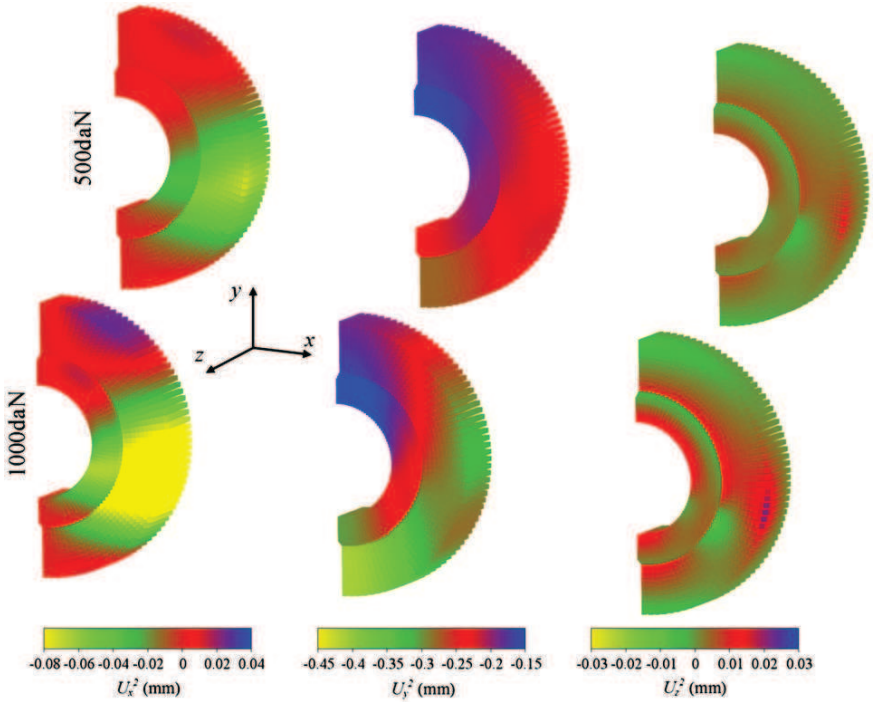

Fig. 12. Distribution of simulated displacement components ($\underline{U}^2$) by considering a deformable fitting, a gap between inner ring/outer ring equal to 40 μm and a gap between fitting/outer ring equal to 100 μm.

bearing and observed values are lower than the ones given by model 2. The essential difference between both models is linked to the progressive bending of the fitting, the inner and the outer rings, made possible by the gaps. In the second model, displacements of the order of the gaps are thus possible while they are limited to displacements associated to elastic strains of a continuous part in the first model. For a load of 500 daN, differences around of 40 μm (which is the gap value between both rings) are observed between both models on U_x and U_y components. Furthermore, in the model 2, discontinuities of

40 μm are also observed at the inner/outer ring interface on the U_x component. The second numerical model shows that the contribution of parameters like gaps and fitting bending involves different displacement fields and certainly a different pressure distribution.

6. Comparison of FE model and experimental results

To compare FE model and experimental results, differences of displacements components have been computed. For that, the common area between experimental images and FE model which corresponds to the upper quarter of the bearing has been extracted. Then, to calculate differences, numerical results have been interpolated on the 3D grid which has been employed to compute experimental data by correlation process. To highlight better the differences, a displacement of an average rigid body motion have been subtracted of the experimental displacement field ($U_{X0} = -85\,\mu m$, $U_{Y0} = 180\,\mu m$ and $U_{Z0} = -150\,\mu m$). Fig. 13 shows differences between numerical data obtained from models and the experimental measured displacements for two slices in the volume and along each direction. First, differences are very low for displacements along the direction z because measured values and numerical data of models 1 and 2 are approximately close to zero. For both other directions, there are large differences (around ± 0.08 mm) between experimental data and numerical ones obtained from the model 1. Concerning $\boldsymbol{U}_y$ component, we have to note that differences vary along the thickness. This model does not take into account the deformation of the fitting and significant differences are observed in particular on the side of the bearing whatever the position along the thickness in the volume. By considering boundary conditions corresponding of model 2, differences along x or y between numerical and experimental displacement fields are divided by 3 and are more homogeneous along the thickness than differences obtained with the model 1. Discontinuities appear on the differences given by model 1 and show that parameters and in particular gaps have to be taken into account. In model 2, there are also small discontinuities of U_x and U_y component differences at the interface of the inner and outer rings with a sign inversion which is probably due to the non symmetric deformation of the ring in the experiment.

The comparison between experimental results and FE model gives a validity of the simulated bearing. It has been shown that fitting behaviour and gaps have significant contributions for distortion conditions on spherical interface and on the performances of the bearing. The validated model corresponds now to a more realistic case and enables the calculation of repartitions of stresses and contact pressures within the bearing. Furthermore, model hypotheses and conditions can now be transposed to more complex cases of aeronautical plain bearings.

7. Contact pressure distribution

Comparison between experimental and simulated displacement fields enabled to modify the initial FE model and to validate it in order to obtain a final FE model which is more realistic. Thus, it is possible to observe stress or contact pressure repartition within the bearing from this validated model. Fig. 14 shows contact pressure distribution in the bearing obtained with initial and final models.

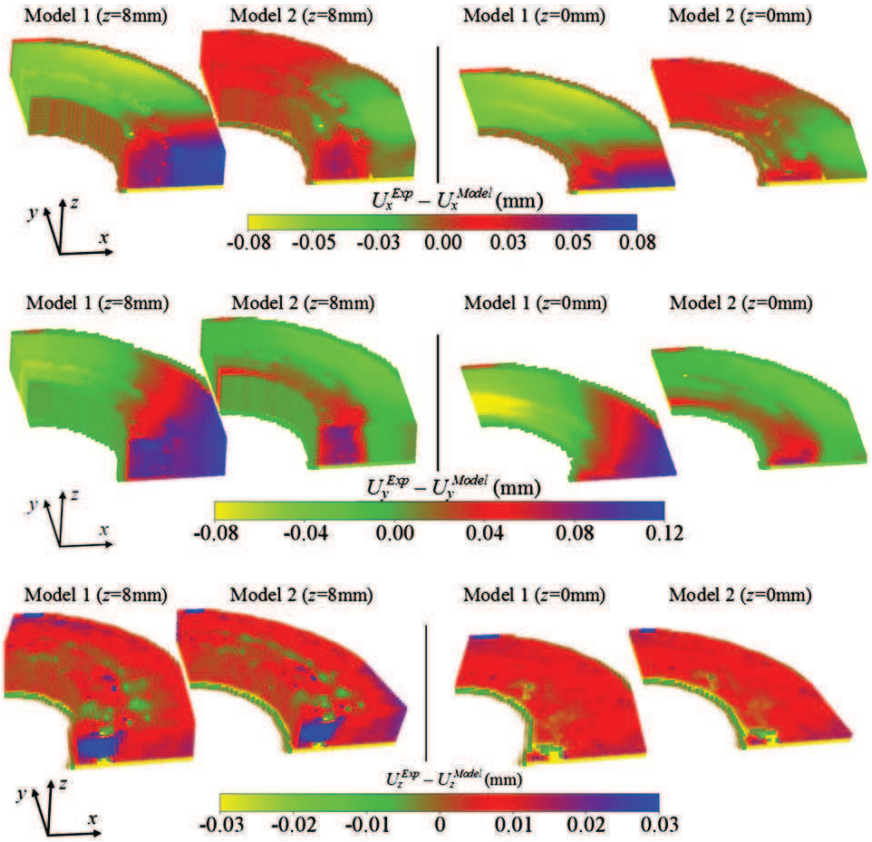

Fig. 13. Differences between numerical displacement and experimental measured displacement fields obtained by model 1 (rigid fitting) and model 2 (deformable fitting) for two slices along the z-direction.

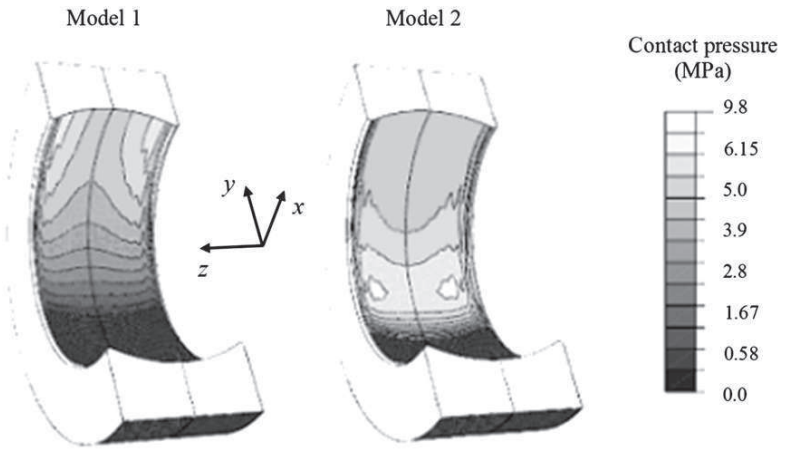

Fig. 14. Contact pressure distribution obtained from the initial FE model 1 and the validated model 2.

Boundary conditions between models, in particular fitting rigidity, change completely pressure distribution. The location of maximal pressure is different. Indeed, fitting deformation induces higher compression on each side of the bearing than in the load axis. With the model corresponding to a realistic case (Fig. 14b), pressure distribution is not ellipsoidal but radically different with maximal pressure located on the sides of the bearing and along the perpendicular direction according to the loading axis.

8. Conclusion

In this paper, a 3D analysis of mechanical behaviour of plain bearing is presented. This problem deals with the pressure distribution on the spherical surface of the bearing. A numerical model has been built and validated from a comparison with 3D experimental measurements of kinematic components. For that, DVC coupled with OST has been employed to study mechanical response of a plain bearing specimen made in epoxy resin. 3D displacement fields have been measured during the loading and these experimental results have been compared with the ones obtained from simulated model. This comparison enabled to study the contribution of various boundary conditions to build the FE model. Some factors have been highlighted like the fitting behaviour which can radically change contact pressure distribution. Furthermore, insertion of gaps between each element of the bearing also improves the numerical model to be a better realistic representation of experimental results. This work shows the significance of the consideration of a representative mechanical environment to study precisely mechanical response of aeronautical plain bearings.

References

[1] Dupré JC, Lagarde A. Photoelastic analysis of a three-dimensional specimen by optical slicing and digital image processing. Exp Mech 1997;37(4):393–7.
[2] Bay BK, Smith TS, Fyrhie DP, Saad M. Digital volume correlation: three-dimensional strain mapping using X-ray tomography. Exp Mech 1999;39(3):217–26.
[3] Verhulp E, Rietbergen B, Huiskes R. A three-dimensional digital image correlation technique for strain measurements in microstructures. J Biomech 2004;37:1313–20.
[4] Germaneau A, Doumalin P, Dupré JC. Full 3D measurement of strain field by scattered light for analysis of structures. Exp Mech 2007;47(4):523–32.
[5] Germaneau A, Doumalin P, Dupré JC. 3D strain field measurement by correlation of volume images using scattered light: recording of images and choice of marks. Strain 2007;43(3):207–18.
[6] Germaneau A, Peyruseigt F, Mistou S, Doumalin P, Dupré JC. Verification of a spherical plain bearing finite-element model using scattered light photoelasticity tests. J Eng Tribol 2008;222(5):647–56.
[7] Hertz H. Ueber die Berührung fester elastischer Körper, Ueber die Berührung fester elastischer Körper und über die Härte. Gesammelte Werke 1881:155–96.
[8] Johnson KL. Contact mechanics. Cambridge: Cambridge University Press; 1985.
[9] Yew A, Jagatia M, Ensaff H, Jin ZM. Analysis of contact mechanics in McKee–Farrar metal-on-metal hip implants. Proc IMechE Part H: J Eng Med 2003;217(5):333–40.
[10] Chu TC, Ranson WF, Sutton MA, Peters WH. Applications of digital image correlation techniques to experimental mechanics. Exp Mech 1985;25(3):232–44.
[11] Bruck HA, McNeill SR, Sutton MA, Peters WH. Digital image correlation using Newton–Raphson method of partial differential correction. Exp Mech 1989;29(2):261–7.
[12] Vendroux G, Knauss WG. Submicron deformation filed measurements: part 2. Improved digital image correlation. Exp Mech 1998;38(2):86–92.
[13] Bornert M, Doumalin P. Micromechanical applications of digital image correlation techniques. In: Jacquot P, Fournier J, editors. Interferometry in speckle light, theory and applications. Springer; 2000. p. 67–74.
[14] Garcia D, Orteu JJ, Penazzi L. A combined temporal tracking and stereo-correlation technique for accurate measurement of 3D displacements. J Mater Proc Technol 2002;125–126:736–42.
[15] Schreier HW, Garcia D, Sutton MA. Advances in light microscope stereo vision. Exp Mech 2004;44(3):278–88.
[16] ABAQUS Analysis User's Manual, version 6.6-1, ABAQUS Inc., 2006.
[17] Bretagne N, Valle V, Dupré JC. Development of marks tracking technique for strain field and volume variation measurement. NDT&E Int 2005;38:290–8.